Article

Permeability of Magnetic Cores with Air Gaps

Yuri N. Starodubtsev [1,2], **Vladimir S. Tsepelev** [1,*], **Vladimir Ya. Belozerov** [2] **and Viktor A. Zelenin** [2]

1   Research Center for Physics of Metal Liquids, Ural Federal University, 620002 Yekaterinburg, Russia;
    iu.n.starodubtsev@urfu.ru
2   Gammamet Research and Production Enterprise, 620131 Yekaterinburg, Russia;
    gammamet@gammamet.ru (V.Y.B.); zwa42523@mail.ru (V.A.Z.)
*   Correspondence: v.s.tsepelev@urfu.ru

Abstract: The influence of the geometric dimensions of the cut core and the number and size of air gaps on the effective permeability was investigated. Using dimensional analysis, an equation was obtained that relates the permeability of the cut core to the simplest dimensionless combination of the mean magnetic flux length l, single air gap length l_{g1}, the cross-sectional area S of the core, and gap number n_g. Permeability calculated from the geometric parameters of the cut core was compared with the effective permeability obtained using a two-dimensional FEMM simulation. Simulation has shown that the equation derived from dimensional analysis provides the best fit. The influence of each significant parameters l, l_{g1}, n_g, and S on cut core permeability is demonstrated. Experimental results have shown that an equation derived from dimensional analysis can be used to predict cut core permeability. In this case, one should take into account the residual air gap that forms after cutting the core. A method for assessing the residual air gap is proposed.

Keywords: permeability; FEMM simulation; nanocrystalline cut core; air gap; inductor

1. Introduction

Nanocrystalline cores are made from an amorphous metal tape with a thickness of about 20 μm. A tape with an amorphous structure is obtained by rapidly quenching a multicomponent melt on the surface of a rotating cooler drum [1]. To obtain a nanocrystalline structure, the tape-wound cores are annealed. Currently, a nanocrystalline soft magnetic material has been widely used that has a composition close to the classical Finemet $Fe_{73.5}Cu_1Nb_3Si_{13.5}B_9$ [2]. In this alloy, Si and B contribute to the formation of an amorphous structure in rapidly quenched tape [3]. Copper provides fine copper-rich clusters, which create a chemical inhomogeneity of the amorphous matrix at the initial stage of annealing. These clusters are centers of nucleation of a large number of α-FeSi nanocrystals. Niobium inhibits the growth of the crystals to a higher temperature and provides a nanocrystalline structure with an average grain size of about 10 nm [4]. Instead of or together with Nb, other elements are used as inhibitors, for example, Mo, W, and V, which change the kinetics of heat release during crystallization [5] and contribute to obtaining the best magnetic properties during heat treatment of cores.

High permeability is associated with a weakening of the macroscopic magnetic anisotropy in the nanoscale structure of the material [6]. Iron-based nanocrystalline soft magnetic materials, in addition to high permeability, have high saturation magnetization. Nanocrystalline soft magnetic material has typical values of coercive force $H_c = 0.5$ A·m^{-1}, initial permeability $\mu_i = 100{,}000$, magnetic induction $B_{800} = 1.3$ T, and loss $P_{0.2/20{,}000} = 0.4$ W·kg^{-1}. The combination of high permeability and saturation magnetization has provided widespread usage in power electronics [7,8] (pp. 277–345).

In a power electrical circuit, inductors are used to store and transmit electromagnetic energy. The magnetic energy of the core W (J) in an external magnetic field H_e (A·m^{-1}) is described as follows:

$$W = \frac{BH_e}{2}V, \tag{1}$$

where B is the magnetic induction (T), and V is the core volume (m^3). Magnetic induction and external magnetic field are related by the following relationship:

$$B = \mu_s\mu_0 H_e, \tag{2}$$

where μ_c is the core permeability, and μ_0 is the magnetic constant (H·m^{-1}). From (1) and (2), we obtain magnetic energy in the following form.

$$W = \frac{B^2}{2\mu_s\mu_0}V. \tag{3}$$

Consequently, with a constant volume V, the magnetic energy stored in the inductor is greater in the core with high magnetic induction and low permeability. It is important to note that magnetic energy is higher in the core in which permeability is constant.

If an external magnetic field is created by winding with current I (A) and the number of turns w, then the external field H_e can be found from Ampere's circuital law:

$$H_e l = Iw, \tag{4}$$

where l is the magnetic path length (m). Using Ampere's law (4), we express magnetic energy in terms of electrical quantities:

$$W = \frac{\mu_s\mu_0 H_e^2}{2}V = \frac{\mu_s\mu_0 Sw^2}{2l}I^2 = \frac{LI^2}{2}, \tag{5}$$

where L is the inductance (H):

$$L = \frac{\mu_s\mu_0 Sw^2}{l}, \tag{6}$$

and the core volume is as follows:

$$V = Sl, \tag{7}$$

where S is the cross-sectional area of a core (m^2).

An inductor as an element of an electrical circuit is characterized by an inductance L and an electric current I. An inductor as a design element is characterized by the dimensions of the core S and l, the permeability of the core μ_c, and the number of turns w. The design quantities are unknown, and they must be found in order to provide the specified values of L and I. From (2) and (4), we find the following.

$$\frac{l}{\mu_s w} = \frac{\mu_0 I}{B}. \tag{8}$$

After substituting (8) into (6), we obtain the following.

$$Sw = \frac{LI}{B}. \tag{9}$$

Relations (8) and (9) represent a system of equations for determining the design parameters of the inductor. On the left side of the equations, there are unknown quantities, and on the right side, there are quantities that are determined by the design of the power circuit. Magnetic induction can be attributed to a limited specified value, since it is limited from the above by the saturation magnetization. Another limitation for B is the overheating temperature of the inductor, which is related core and winding losses. From (8) and (9), it follows that a decrease in magnetic induction results in an increase in the core's

size. It is impossible to unambiguously calculate the inductor; therefore, the successive approximation is used to optimize the inductor's design.

An important advantage of nanocrystalline soft magnetic materials as an inductor core is low loss and high saturation magnetization. For the thermally limited design of the inductor, these advantages allow one to obtain a high working induction and a small core size.

Low permeability is obtained by creating air gaps in the core. In a closed core, the magnetic flux is concentrated in the magnetic material. Air gaps redistribute the magnetic flux so that part of it is scattered near the gap. Magnetic flux extends beyond the core cross-section, creating a fringing flux [9,10]. Effective permeability of the core with air gaps depends on geometric dimensions of the core (S and l), as well as on the single air gap length l_{g1} and the number of gaps n_g. Since all these quantities strongly affect core losses [11–13], optimization of the number and size of air gaps in the inductor core is an important design problem.

2. Materials and Methods

Two-dimensional finite element modeling software FEMM 4.2 was used to simulate the effective permeability of annular core with air gaps [14]. A winding of 8 turns with a current of 3 A was uniformly applied to the annular core. The calculated effective permeability μ_{BH} represented the ratio of the average normal magnetic induction B_n in the magnetic cut core and in the same core filled with air. For the calculation, we used the magnetization curve of a composite core made of nanocrystalline soft magnetic alloy $Fe_{72.5}Cu_1Nb_2Mo_{1.5}Si_{14}B_9$ [8] (p. 265). In a composite core, all magnetic quantities are referred to the unit of the geometric cross-section of the core. The magnetic induction in a field of 800 A $\times$ m^{-1} is 0.83 T, the initial permeability is 40,000, and the maximum permeability is 380,000. For experimental studies, cut cores made of the same magnetic material were used. Experimental effective permeability μ_L was calculated from the inductance of the winding uniformly applied to the core (see Formula (6)). Inductance was measured at 1 kHz using an E7-22 RLC meter (Chy Firemate Co., Ltd., Tainan City, Taiwan).

3. Theory

We will distinguish between core permeability μ_c of the following:

$$\mu_s = \frac{B}{\mu_0 H_e},\tag{10}$$

and the permeability of the magnetic material μ.

$$\mu = \frac{B}{\mu_0 H_i}.\tag{11}$$

In Formulas (10) and (11), H_e is the external magnetic field, and H_i is the internal magnetic field. Thus, the quantity of μ determines the property of the magnetic material and the quantity of μ_c determine the properties of the core, i.e., an object that has a well-defined geometry and is made of a magnetic material.

Internal and external fields are related by the following relation [15]:

$$H_i = H_e - NM,\tag{12}$$

where M is magnetization (A·m^{-1}), and N is the demagnetization factor. From (12), we find the following external field:

$$H_e = H_i + N\left(\frac{B}{\mu_0} - H_i\right),\tag{13}$$

by considering the following:

$$B = \mu_0(M + H_i),$$ (14)

and substitute (13) in (10).

$$\mu_s = \frac{B}{\mu_0 H_i + N(B - \mu_0 H_i)} = \frac{\mu}{1 + N(\mu - 1)}.$$ (15)

If material permeability μ is much greater than 1, then (15) can be reduced to the following form.

$$\frac{1}{\mu_s} = \frac{1}{\mu} + N.$$ (16)

It follows from (16) that, in the limit $\mu \to \infty$, core permeability is inversely proportional to the demagnetization factor N, i.e., μ_c does not depend on the magnetic material.

Let us calculate the demagnetization factor N of an annular core with a magnetization M, which has n_g gaps of length l_{g1} each. Let us assume that the magnetic flux in the magnetic material and in the air gaps is uniform, and there is no electric current. If we choose a circle of length l as contour, then, taking into account the magnetic field in the magnetic material $-NM$ and in air gap M, from (4), we obtain the following.

$$- NM(l - n_g l_{g1}) + M n_g l_{g1} = 0.$$ (17)

From (17), we find the demagnetization factor of a magnetic contour of length l with cuts:

$$N = \frac{l_g}{l - l_g},$$ (18)

where $l_g = n_g l_{g1}$ represent the total air gap. Since Formula (18) was obtained for a contour, it is valid for a thin annulus in which the cross section is $S \to 0$, with uniform magnetization inside the ferromagnet (the density of volume magnetic charges is zero) and the absence of magnetic scattering near the air gap, that is, for a small air gap when $l_g \ll l$.

After substituting (18) into (15), we obtain the following.

$$\mu_c = \frac{\mu}{1 + (\mu - 1)\frac{l_g}{l - l_g}}.$$ (19)

Figure 1 shows the dependences of the core permeability μ_c on the ratio of the air gap length l_g to the length of the magnetic part of the core $(l - l_g)$, calculated by formula (19). The dashed straight line in Figure 1 corresponds to the following equation.

$$\mu_c = \frac{l - l_g}{l_g}.$$ (20)

Starting from a certain value $l_g \times (l - l_g)^{-1}$, core permeability depends only on geometric parameters. For $l_g \ll l$, instead of (20), one can use the following equation.

$$\mu_c = \frac{l}{l_g}.$$ (21)

In order to determine the relationship between the permeability and the geometric parameters of the cut core, we will use dimensional analysis. Core permeability μ_c is a dimensionless quantity that decreases with an increase in the number of gaps, n_g, the length of single gap, l_{g1}, the cross-sectional area of the core S, and also with a decrease in the mean magnetic path length, l. This makes it possible to relate core permeability μ_c with the simplest dimensionless combination of these significant geometric quantities in the following form.
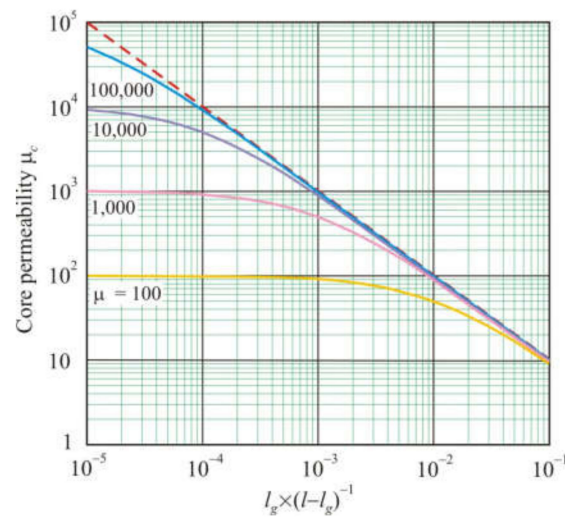
Figure 1. Dependences of the annular core permeability μ_c on the $l_g \times (l - l_g)^{-1}$ ratio for magnetic material with different permeability μ. The dashed line corresponds to equation $\mu_c = l_g \times (l - l_g)^{-1}$.

$$\mu_s = \frac{l}{n_g l_{g1}} + \frac{l}{n_g \sqrt{S}}. \tag{22}$$

Equation (22) can also be written in the following form:

$$\mu_s = \frac{l}{l_g}\left(1 + \frac{l_g}{n_g \sqrt{S}}\right) \tag{23}$$

for independent variables l, l_g, n_g, and S, where $l_g = l_{g1} n_g$ is the total air gap, and also in the following form:

$$\mu_s = \frac{l}{l_g}\left(1 + \frac{l_{g1}}{\sqrt{S}}\right) \tag{24}$$

for independent variables l, l_g, l_{g1}, and S.

To determine the permeability of a cut core, designers usually use the following relationship [9,10]:

$$\mu_c = F\frac{l}{l_g}, \tag{25}$$

where F is the fringing flux factor:

$$F = 1 + \frac{l_g}{n_g \sqrt{S}} \ln\left(\frac{l_w}{l_g}\right), \tag{26}$$

and l_w is the length of the winding applied to the core. If the winding is applied uniformly along the entire length of the core, then $l_w = l$. Equation (25) was first obtained by Partridge [16].

Next, we will evaluate the applicability of Equations (21), (22), and (25) for calculating the permeability of cut cores.

4. Simulation

Figure 2 shows the relationship of the permeability μ_{geo} calculated from Equations (21), (22), and (25), which includes only the geometric parameters of the core, with effective permeability μ_{BH} obtained using two-dimensional FEMM simulations. Annular cores 100×60 mm

in size had one air gap with a length of 1×10^{-4} to 1.28×10^{-2} m. The mean magnetic path length was taken as follows:

$$l = \frac{\pi(D_o + D_i)}{2},$$ (27)

where D_e is the outer diameter, and D_i is the inner diameter of core. The effective magnetic path length l_{ef} is determined by the following formula.

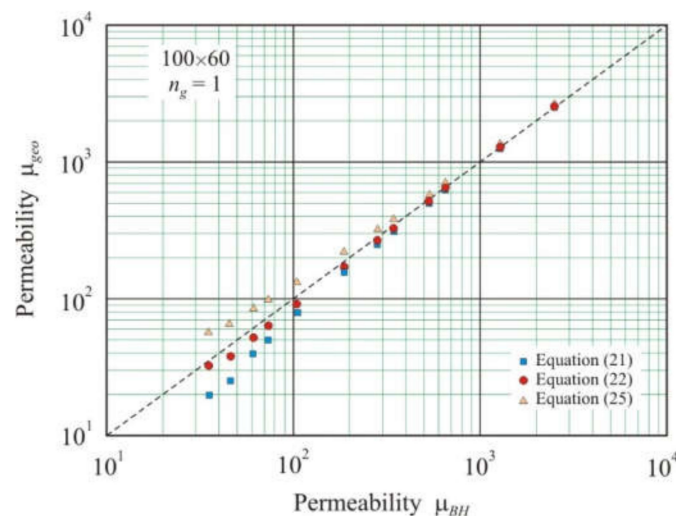$$l_{ef} = \frac{\pi(D_o - D_i)}{\ln \frac{D_o}{D_i}}.$$ (28)

Figure 2. Relationship between geometric permeability μ_{geo} calculated by Equations (21), (22), and (25) and effective permeability μ_{BH} obtained using FEMM simulation in soft magnetic annuluses 100×60 mm with one air gap of length l_{g1} from 1×10^{-4} to 1.28×10^{-2} m. The dashed line corresponds to equation $\mu_{geo} = \mu_{BH}$.

For a 100×60 core, Formulas (27) and (28) provide magnetic path lengths that differ by only 2%.

As a cross-section area of the core for two-dimensional modeling, we used the following.

$$\sqrt{S} = \frac{D_o - D_i}{2}.$$ (29)

For a planar core, $l_{g1} \times S^{-0.5}$ in Equation (24) represents the ratio of the length of a single air gap to its width.

From Figure 2, it follows that, at a small gap (high permeability), the geometric permeability μ_{geo} is close for all three Equations (21), (22), and (25), and these values are in good agreement with effective permeability μ_{BH}. As the gap increases, the discrepancy between the different equations increases. Partridge Equation (25) overestimates permeability, and simple ratio (21) underestimates. Equation (22) obtained from dimensional analysis has the smallest deviation from the straight line $\mu_{geo} = \mu_{BH}$. This linear relationship on the logarithmic scale has a highly adjusted coefficient of determination $R^2_{adj} = 0.9995$. The deviation from the straight line $\mu_{geo} = \mu_{BH}$ characterizes the exponent $s = 1.04$ in the power function.

$$\mu_{geo} \propto \mu_{BH}^s.$$ (30)

As the number of gaps increases, the convergence of μ_{geo} and μ_{BH} improves. Figure 3 shows the relationship between the geometric permeability μ_{geo}, calculated from Equations (21), (22),

and (25), and the effective permeability μ_{BH} for annular cores of 100×60 mm with four air gaps. The best convergence is shown by Equation (22) with the coefficient of determination $R^2_{adj} = 1$ and exponent $s = 1.01$.
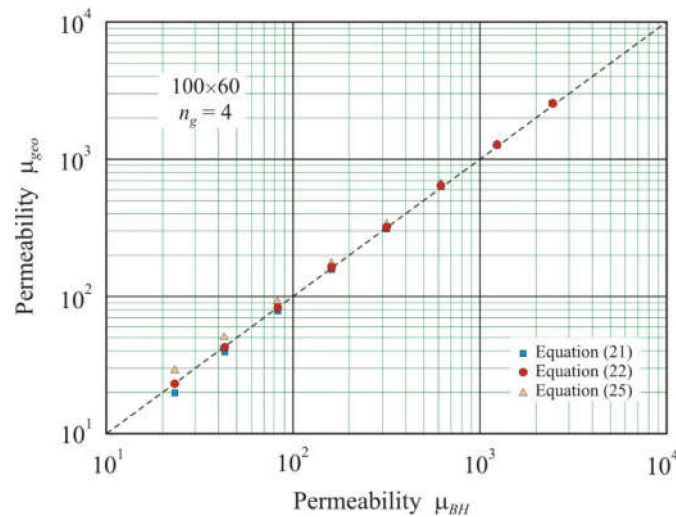

Figure 3. Relationship between geometric permeability μ_{geo} calculated by Equations (21), (22), and (25) and effective permeability μ_{BH} obtained using FEMM simulation in soft magnetic annuluses 100×60 mm with four air gaps and total length l_g from 1×10^{-4} to 1.28×10^{-2} m. The dashed line corresponds to equation $\mu_{geo} = \mu_{BH}$.

If we take cores with the same l, S, and n_g, then, in accordance with (22), core permeability should be reciprocal relative to total air gap l_g^{-1}. Figure 4 shows the dependence of the effective permeability μ_{BH} on l_g for 100×60 cores with $n_g = 1$, 2, and 4. It can be seen that for cores with four gaps, the dependence on the logarithmic scale is linear with the coefficient of determination $R^2_{adj} = 0.9997$ and the exponent $s = -0.97$ for power function (30). With a decrease in the number of gaps, nonlinearity increases, and it is particularly significant for large l_g. Nonlinearity is affected by the second term of the sum in Equation (22), which increases with a decreasing number of gaps.
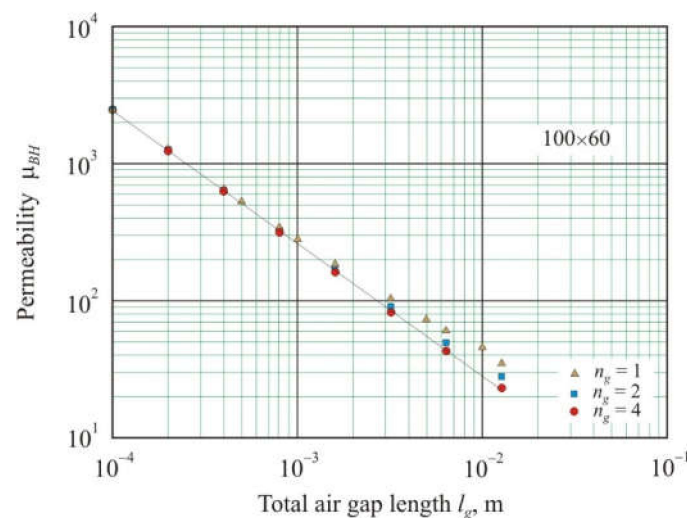

Figure 4. Relationship of effective permeability μ_{BH} with the total length of air gaps l_g in soft magnetic annuluses of 100×60 mm with the number of air gaps $n_g = 1$, 2, and 4.

Figure 5 shows the distribution of the normal magnetic induction B_n averaged over the cross-section of a 100×60 annular core depending on the angular coordinate. Cores with

n_g = 1, 2 and 4 air gaps had the same total air gap length $l_g = 6.4 \times 10^{-3}$ m. The smallest magnetic flux density in Figure 5 corresponds to the middle of the air gap. It can be seen that with an increase in the number of gaps, magnetic flux becomes more uniform along the length of the core, and at the same time, average magnetic induction and, consequently, permeability decrease.
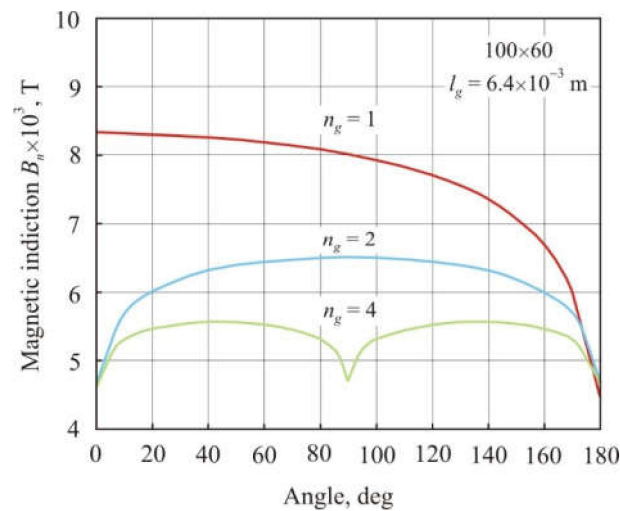

Figure 5. Distribution of normal magnetic induction B_n averaged over the cross-section of an annular core 100 × 60 mm depending on the angular coordinate. The cores had the same total air gap length $l_g = 6.4 \times 10^{-3}$ with the number of gaps n_g = 1, 2, and 4.

The decrease in permeability with an increase in the number of gaps with constant l, S, and l_g follows from Equation (22). Figure 6 shows the dependence of the effective permeability μ_{BH} on the reciprocal of air gap number n_g^{-1} in annular cores of 100 × 60 mm with a total air gap length $l_g = 6.4 \times 10^{-3}$ m. The number of gaps in the cores n_g = 1, 2, 4, 8, and 16. The dependence of μ_{BH} on n_g^{-1} is linear with the coefficient of determination R^2_{adj} = 0.998.
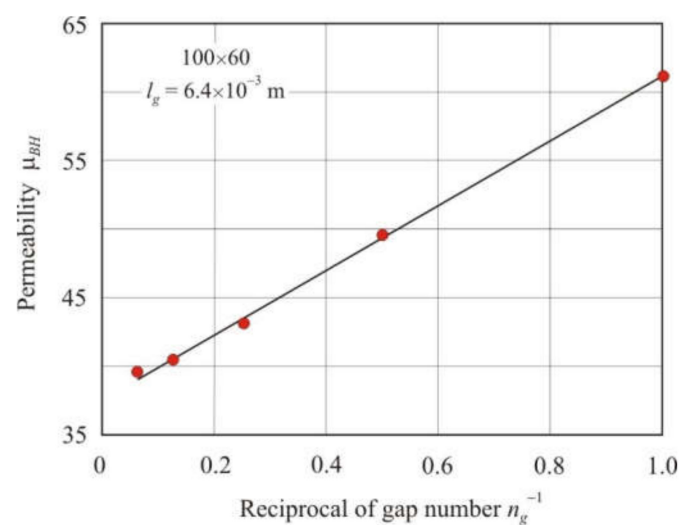

Figure 6. Dependence of the effective permeability μ_{BH} on the reciprocal of air gap number n_g^{-1} in soft magnetic annuluses 100 × 60 mm with the total air gap length $l_g = 6.4 \times 10^{-3}$ m.

From Equation (22), it follows that with constant l, l_g, and n_g, core permeability is linearly related to $S^{-0.5}$, where S is the cross-section area of the core. Figure 7 shows the dependence of the effective permeability μ_{BH} on $S^{-0.5}$ in annular cores with two air gaps,

the mean magnetic path length $l = 0.08$ m, and the total air gap length $l_g = 6.4 \times 10^{-3}$ m. The dependence of μ_{BH} on $S^{-0.5}$ is linear with the coefficient of determination being $R^2_{adj} = 0.998$.
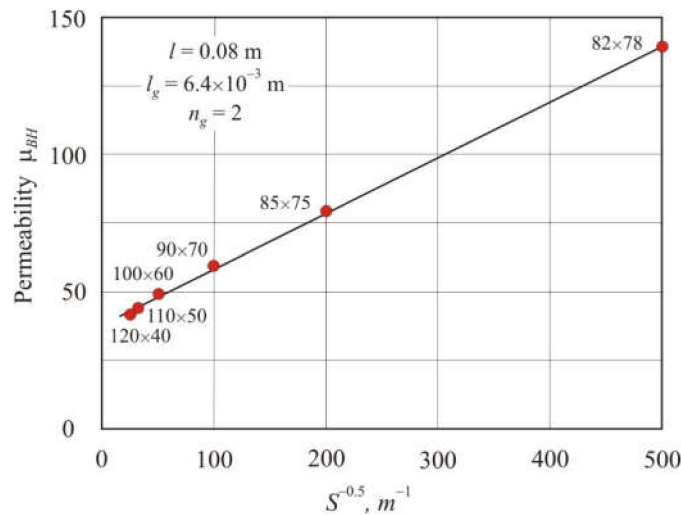

Figure 7. Dependence of the effective permeability μ_{BH} on $S^{-0.5}$ in soft magnetic annuluses with two air gaps, the mean magnetic flux length $l = 0.08$ m and the total air gap length $l_g = 6.4 \times 10^{-3}$ m. Core dimensions are shown near points.

Comparing cores with different cross-section areas allows us to return again to Equations (21), (22), and (25). Figure 8 shows the relationship between geometric permeability μ_{geo}, calculated from Equations (21), (22), and (25), and effective permeability μ_{BH} for 82×78 mm annular cores with four air gaps and the total air gap length from 1×10^{-4} to 1.28×10^{-2} m. Comparison of cores 100×60 mm (Figure 3) and 82×78 mm (Figure 8), which have the same l, l_g, and the number of gaps $n_g = 4$ but different cross-section areas shows that in a core with a small cross-section, the convergence of geometric permeability μ_{geo} with effective permeability μ_{BH} is noticeably worse. Despite this, Equation (22) again provides the best results with the coefficient of determination $R^2_{adj} = 0.998$ and exponent $s = 1.02$ for the power function.
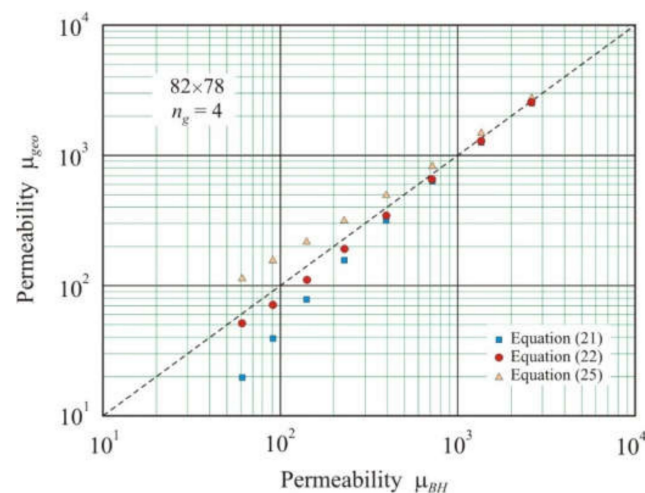

Figure 8. Relationship between geometric permeability μ_{geo} calculated by Equations (21), (22), and (25) and effective permeability μ_{BH} obtained using FEMM simulation in soft magnetic annuluses 82 $\times$ 78 mm with four air gaps and total length l_g from 1×10^{-4} to 1.28×10^{-2} m. The dashed line corresponds to equation $\mu_{geo} = \mu_{BH}$.

Figure 9 shows the distribution of normal magnetic induction B_n averaged over the cross-section of annular cores 100 × 60 mm and 82 × 78 mm depending on the angular coordinate. The cores were in an external magnetic field of 97 A × m^{-1}. They have the same l = 0.08 m, l_g = 6.4 × 10^{-3} m, and the number of gaps n_g = 4 but differ in the ratio $l × S^{-0.5}$. Four air gaps divide the core into four magnetic pieces. The $l × S^{-0.5}$ ratio in the 82 × 78 mm core is 10-times greater than in the 100 × 60 mm core. It follows from Figure 8 that the magnetic induction in the 82 × 78 mm core is much higher and is more nonuniformly distributed along the length of the core. This is consistent with the results of calculating the demagnetizing factor N for rectangular prisms [17], which decreases with an increase in ratio $l × S^{-0.5}$. A decrease in N promotes the convergence of the internal and external magnetic fields and an increase in magnetic induction and core permeability (see Equation (16)).
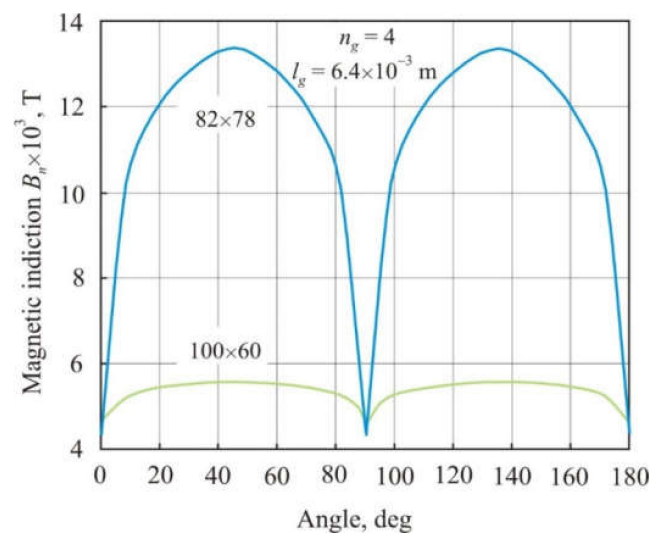

Figure 9. Distribution of normal magnetic induction B_n averaged over the cross-section of annular cores 100 × 60 mm and 82 × 78 mm depending on the angular coordinate. The cores have the same mean magnetic path length l = 0.08 m, the total air gap length l_g = 6.4 × 10^{-3} m, and the number of gaps n_g = 4.

5. Experiment

After cutting the nanocrystalline core in half and then compressing the two halves tightly, core permeability decreases. This indicates that a residual air gap has formed in the core. The length of the residual air gap l_o can be found by taking into account that after tight compression, condition $l_o \ll l$ is satisfied. In this case, from (21), we have the following:

$$l_o = \frac{l}{\mu_L}, \tag{31}$$

where μ_L is the measured permeability of the core after cutting and tight compression. For a more accurate determination of the residual air gap length, Equation (23) can be used, from which the following is obtained.

$$l_o = \frac{l}{\mu_L - \frac{l}{n_g \sqrt{S}}}. \tag{32}$$

For most of the cores in this study, Equations (31) and (32) produce similar results.

Figure 10 shows the dependence of the residual air gap length l_o on cross-sectional area S after cutting various nanocrystalline cores in half and then tightly compressing the two halves. The residual air gap length was calculated from Equation (32). It follows from Figure 10 that with an increase in the cross-section area, the residual air gap length

grows. The linear relationship between l_o and S on a logarithmic scale has a coefficient of determination $R^2_{adj} = 0.78$ and can be represented as a power function:

$$l_{o1} = 0.00125 \times S^{0.34}, \tag{33}$$

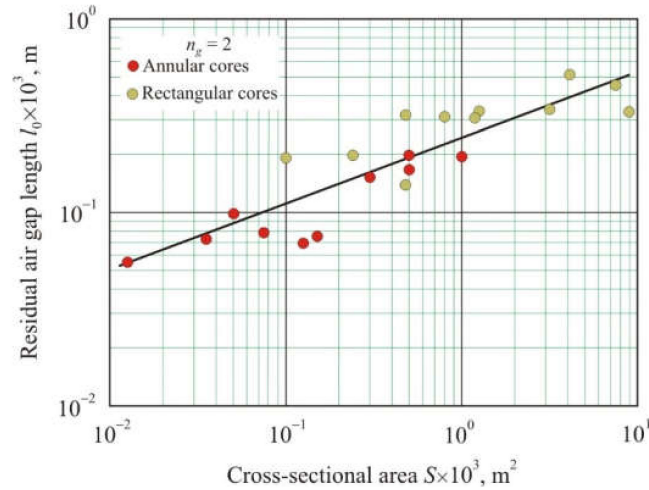where l_{o1} is the single residual air gap length.

Figure 10. Dependence of the residual air gap length l_o on the cross-sectional area S after cutting the nanocrystalline core in half and then tightly compressing the two halves.

Figure 11 shows the effect of the residual air gap on the permeability of the cut core. The $60 \times 125 \times 90$ (100) rectangular core had two air gaps. Figure 12 shows the dimensions of a rectangular core with a general dimensional formula $a \times b \times h$ (c). Spacers were inserted into the air gaps. The spacer thickness l_s was varied from 0.3 to 9.8 mm. The geometric permeability of the core μ_{geo} was calculated using Equation (23). The total air gap length l_g was taken equal to l_s or $(l_s + l_o)$. The total residual air gap $l_o = 0.454$ mm was calculated using Equation (32). Geometric permeability μ_{geo} was compared with measured permeability μ_L. Figure 11 shows that the permeability prediction accuracy of the cut core is significantly improved when the residual air gap is taken into account. If the fraction of the residual air gap is small, then the calculated and measured permeabilities are in good agreement.
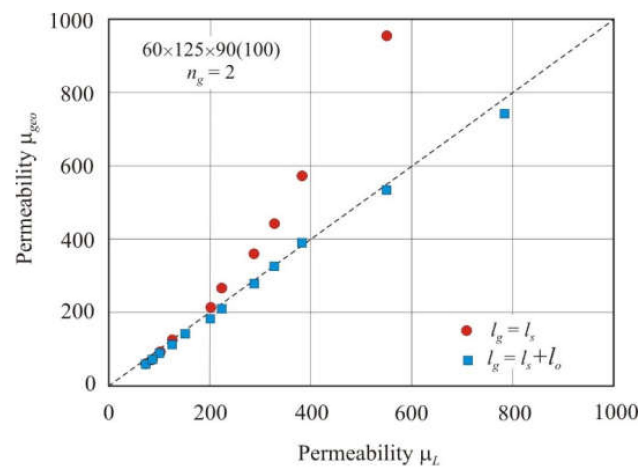

Figure 11. Relationship of geometric permeability μ_{geo} and measured permeability μ_L in a $60 \times 125 \times 90$ (100) rectangular core with two air gaps. The total air gap length l_g was taken equal to l_s or $(l_s + l_o)$, where l_s is the spacer thickness, and l_o is the residual air gap length. The dashed line corresponds to equation $\mu_{geo} = \mu_L$.
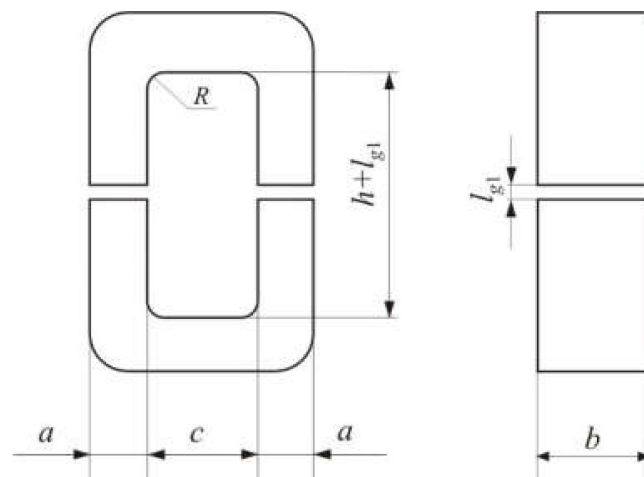
Figure 12. Dimensions of a rectangular core with a general dimensional formula $a \times b \times h$ (c).

Figure 13 shows the relationship of geometric permeability μ_{geo} with the measured permeability μ_L in different nanocrystalline rectangular cores with two gaps. Permeability μ_{geo} was calculated using Equation (23). Spacers were inserted into the gaps, and the total air gap length l_g was taken equal to ($l_s + l_o$). The linear relationship between the calculated and measured permeabilities has a high coefficient of determination $R^2_{adj} = 0.993$ and an exponent $s = 0.96$ in the power function.
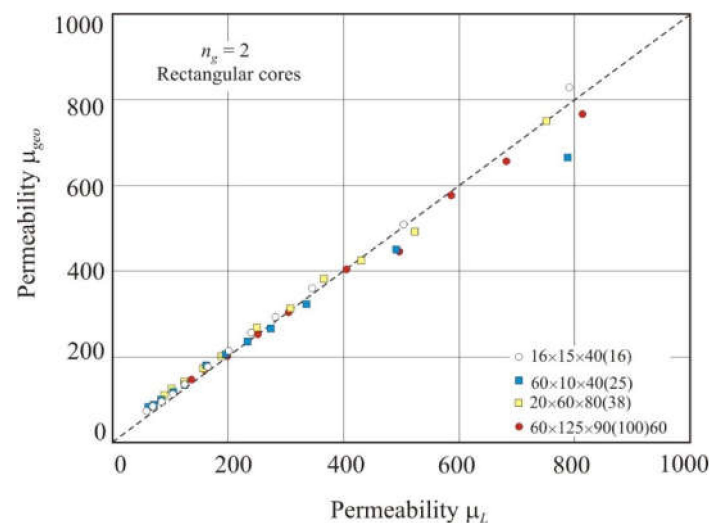

Figure 13. Relationship between geometric permeability μ_{geo} and measured permeability μ_L in nanocrystalline rectangular cores with two air gaps. The total air gap length l_g was taken equal to ($l_s + l_o$), where l_s is the spacer thickness, and l_o is the residual air gap length. The dashed line corresponds to equation $\mu_{geo} = \mu_L$.

Figure 14 shows the relationship of the geometric permeability μ_{geo} with the measured permeability μ_L in different nanocrystalline annular cores with 8 or 14 air gaps. Spacers were inserted into the gaps, and the air gap was equal to the sum ($l_s + l_o$). The linear relationship between the calculated and measured permeabilities was worse than in the cores with two gaps. The coefficient of determination R^2_{adj} of this linear dependence is 0.96, and the exponent is $s = 0.90$ in the power function.
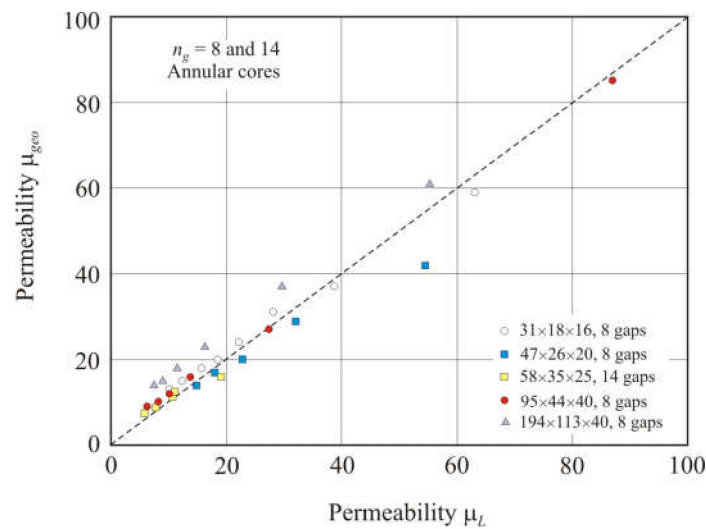
Figure 14. Relationship between geometric permeability μ_{geo} and measured permeability μ_L in nanocrystalline annular cores with 8 or 14 air gaps. The total air gap length l_g was taken equal to $(l_s + l_o)$, where l_s is the spacer thickness, and l_o is the residual air gap length. The dashed line corresponds to equation $\mu_{geo}= \mu_L$.

Experimental results demonstrate that Equation (22) can be used to accurately predict the permeability of a cut core. In practice, an account should be taken of the residual air gap that forms after the core is cut. A method for estimating the residual air gap length is proposed. The method takes into account that the scattering of the magnetic flux will be minimal when individual magnetic pieces of the cut core are tightly compressed.

6. Conclusions

Cut core permeability is a dimensionless quantity, which decreases with an increase in the number of air gaps n_g, single gap length l_{g1}, cross-sectional area S of the core, and also with a decrease in the mean magnetic flux length l. Using dimensional analysis, an equation was obtained that relates cut core permeability to the simplest dimensionless combination of these significant geometric quantities. The equation has a simpler form in comparison with the traditional Partridge equation.

Permeability μ_{geo}, calculated from the geometric parameters of the cut core, was compared with the effective permeability μ_{BH} obtained using a two-dimensional FEMM simulation. Simulation has shown that the equation derived from dimensional analysis provides the best fit for μ_{geo} and μ_{BH}. As the gap number increases, the convergence of these permeabilities improves. The influence of each of the significant parameters l, l_{g1}, n_g, and S on the cut core permeability is demonstrated. It is shown that significant geometric parameters affect permeability according to an equation derived from dimensional analysis.

Experimental results have shown that an equation relating permeability to geometric parameters can be used to predict the cut core permeability. In practice, account should be taken on the residual air gap that forms after the core is cut. A method for estimating the residual air gap length is proposed. The method takes into account that the scattering of the magnetic flux will be minimal when individual magnetic pieces of the cut core are tightly compressed.

Author Contributions: Conceptualization, V.Y.B.; methodology, Y.N.S.; software, Y.N.S. and V.A.Z.; validation, Y.N.S. and V.S.T.; formal analysis, V.S.T. and Y.N.S.; investigation, Y.N.S. and V.A.Z.; resources, V.S.T. and V.Y.B.; data curation, V.S.T.; writing—original draft preparation, Y.N.S.; writing— review and editing, Y.N.S.; visualization, Y.N.S.; supervision, V.S.T.; project administration, V.S.T. and V.Y.B.; funding acquisition, V.S.T. All authors have read and agreed to the published version of the manuscript.

References

1. Narasimhan, M.C. Continuous Casting Method for Metallic Strips. US Patent 4142571, 6 March 1979.
2. Yoshizawa, Y.; Oguma, S.; Yamauchi, K. New Fe-based soft magnetic alloys composed of ultrafine grain structure. *J. Appl. Phys.* **1988**, *64*, 6044–6046. [CrossRef]
3. Luborsky, F.E.; Becker, J.J.; Walter, J.L.; Liebermann, H.H. Formation and magnetic properties of Fe-B-Si amorphous alloys. *IEEE Trans. Magn.* **1979**, *15*, 1146–1149. [CrossRef]
4. Tsepelev, V.S.; Starodubtsev, Y.N. Nanocrystalline soft magnetic iron-based materials from liquid state to ready product. *Nanomaterials* **2021**, *11*, 00108. [CrossRef] [PubMed]
5. Tsepelev, V.S.; Starodubtsev, Y.N.; Belozerov, V.Y. The effect of inhibitors on the structure and magnetic properties of nanocrystalline soft magnetic alloys. *Phys. Met. Metallogr.* **2018**, *119*, 831–836. [CrossRef]
6. Herzer, G. Nanocrystalline soft magnetic alloys. In *Handbook of Magnetic Materials*; Buschow, K.H.J., Ed.; Elsevier: Amsterdam, The Netherlands, 1997; Volume 10, pp. 415–462.
7. Hilzinger, R.; Rodewald, W. *Magnetic Materials: Fundamentals, Product, Properties, Applications*; Publicis MCD: Erlangen, Germany, 2013; pp. 467–520.
8. Starodubtsev, Y.N. *Physical Properties and Application of Soft Magnetic Materials*; Hotline–Telecom: Moscow, Russia, 2020.
9. McLyman, C.W.T. *Transformer and Inductor Design Handbook*; Marcel Dekker: New York, NY, USA, 2004; pp. 241–263.
10. Kazimierczuk, M.K. *High-Frequency Magnetic Components*; John Wiley & Sons: Chichester, UK, 2014; pp. 54–57.
11. Fukunaga, H.; Eguchu, T.; Ohta, Y.; Kakehashi, H. Core loss in amorphous cut cores air gaps. *IEEE Trans. Magn.* **1989**, *25*, 2694–2698. [CrossRef]
12. Wang, Y.; Calderon-Lopez, G.; Forsyth, A.J. High-frequency gap losses in nanocrystalline cores. *IEEE Trans. Power Electron.* **2017**, *32*, 4683–4690. [CrossRef]
13. Calderon-Lopez, G.; Wang, Y.; Forsyth, A.J. Mitigation of gap losses in nanocrystalline tape-wound cores. *IEEE Trans. Power Electron.* **2019**, *34*, 4656–4664. [CrossRef]
14. Available online: http://www.femm.info (accessed on 28 November 2021).
15. Chikazumi, S. *Physics of Ferromagnetism*; Oxford University Press: Oxford, UK, 1997; pp. 13–17.
16. Partridge, G.F. The influence of iron-cored coils having an air gap. *Phil. Mag.* **1936**, *22*, 665–678. [CrossRef]
17. Chen, D.-X.; Pardo, E.; Sanchez, A. Demagnetizing factors for rectangular prisms. *IEEE Trans. Magn.* **2005**, *41*, 2077–2088. [CrossRef]